Using Reflections in a Meander Line Turn of Two Segments for Suppressing UWB Excitations

Roman S. Surovtsev, Pavel V. Mikola, Salim Karri, and Ilya A. Ivantsov

Abstract — The article shows the possibility of suppressing ultra-wideband (UWB) pulse effects in structures using the example of a meander line of two segments with different cross-sectional parameters. The proposed structures suppress UWB excitations by their modal decomposition and reflection. As a result of preliminary simulations, we chose two tracing options. The first one uses alignment of the magnitudes of the main interfering modes and their reflections from the junction of the segments. The second option uses simultaneous arrival and mutual compensation of the main and reflected components of interference. The obtained conditions allowed choosing optimal geometric parameters and implementing both structures. The structures were simulated using two approaches: quasi-static and electrodynamic; their results demonstrated good consistency. The first structure attenuates the interference impact by about 3.5 times, and the second by 3.9 times. The calculated eye diagrams allowed evaluating the integrity of useful signals when a pseudo-random binary bit sequence (PRBS) was propagating through the structures. The second structure was found more preferable because it provides higher attenuation rates and is less harmful to the useful signal at higher bit rates. Finally, an example of proposed approach is given.

Index Terms— Electromagnetic compatibility, ultra-wideband excitation, protection, reflections, signal integrity, eye diagram.

I. Introduction

Ensuring protection of radioelectronic equipment (REE) against conductive pulsed electromagnetic interference (EMI) of nanosecond duration is an urgent task of electromagnetic compatibility [1]. The evolution of REE has made them more compact and functional, but also more susceptible to EMI [2]. This is explained by the fact that high speed of REE operation requires increasing the upper frequencies of the signal spectra, which together with the high density of PCB tracing in modern REE leads to a decrease in the noise immunity and an increase in the susceptibility to EMI impact. In addition, the danger of using generators of powerful ultra-wideband (UWB) excitation for intentional destabilization of REE has also significantly increased in recent years [3–5]. A wide spectrum of UWB excitations allows part of their frequency components to overcome the protection devices, penetrate inside the REE, and disturb the digital exchange. Additionally, their high power contributes to REE failure by causing electrical breakdown of semiconductors and dielectrics [6, 7]. This happens because high energy density of UWB excitation during its action does not have time to be transferred to the surrounding elements. As a consequence, there appear defects in the sensitive areas of heat generation. The development of technologies of generating UWB excitations evolved into high power electromagnetic systems (HPEMS). These systems can send directed destructive pulses to the object by controlling its work [8]. Many methods and devices have been proposed to protect important systems against EMI [9–12]. Despite this, the search and research of new ways of protecting REE from various types of EMI are still relevant.

An important component of PCBs is microstrip lines (MSLs). These structures have found wide application for transmission of information signals and power between the functional units of REE electrical circuits [13]. MSLs allow designing a wide range of microwave devices, so their research now is currently topical. One of MSL applications is filtering and protection from EMI [14–18]. The remarkable approach and devices that protect against UWB excitations, proposed in [17, 18], are based on the phenomenon of modal decomposition. The protection principle of these devices is based on the decomposition of interfering signals into components (modes) of lower amplitudes. This decomposition is possible because of the difference in phase velocity of their propagation in the coupled MSLs. Optimizing the coupling between the conductors allows minimizing the amplitude of the components at the output of the strip protection device. Reflections of signals from inhomogeneities in the structures of several segments of such coupled lines together with modal decompositions are an additional resource for attenuating the amplitude of the UWB excitations.

In this paper, we consider a meander line (ML) that consists of two segments with different parameters of the signal conductors and the spacing between them. Presumably, such configuration will allow for the additional attenuation of the UWB amplitude by means of signal reflections from a junction between the ML segments. The purpose of this work is to demonstrate the possibility of using signal reflections to additionally suppress the UWB excitation amplitude.

II. Preliminary Simulation

To demonstrate the effect of reflections on the decomposition of the pulsed excitation, we consider MLs of one and two segments. The cross section of each segment is a coupled two-con-

This work was supported by the Ministry of Science and Higher Education of the Russian Federation, project FEWM-2022-0001. The simulation of time response was funded by the President's Grant, project 396.2022.4 at TUSUR. (Corresponding author: Roman S. Surovtsev). The authors are with the Tomsk State University of Control Systems and Radioelectronics, Tomsk 634050, Russia (e-mail: surovtsevrs@gmail.com).

ductor line (Fig. 1). The connection diagrams of these MLs are shown in Fig. 2 (the routing of the diagram from Fig. 2b will be shown in Section V).

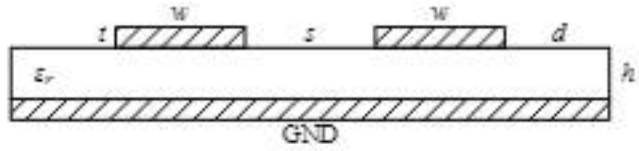

Fig. 1. Cross-section of the ML turn.

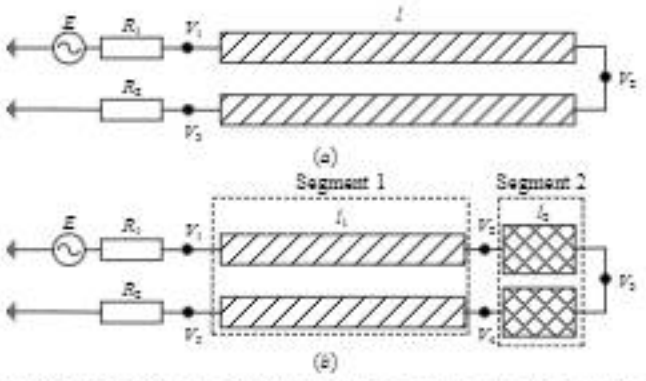

Fig. 2. Circuit diagrams of the ML turn of one (a) and two (b) segments.

In the case of a symmetrical cross-section of the ML turn, the excitation can be decomposed just into two pulses: even and odd modes. For UWB pulse decomposition in the MSL structure, it was necessary to ensure the condition

$$2l(\tau_e-\tau_o) \geq t_\Sigma \qquad (1)$$

where τ_o and τ_e are the per-unit-length delays of the even and odd modes and t_Σ is the sum of the rise (t_r), flat-top (t_{fl}), and fall (t_f) durations of the UWB pulse.

For the two-segment ML turn, we have the condition

$$2l_1(\tau_{e1}-\tau_{o1})+2l_2(\tau_{e2}-\tau_{o2}) \geq t_\Sigma \qquad (2)$$

where subindexes "1" and "2" are introduced to define the number of the ML turn segment.

Simultaneously with conditions (1)–(2), it was necessary to minimize the reflections at the near end of the turns in Fig. 2. The condition for such a minimization is as follows:

$$R_1=R_2=(Z_eZ_o)^{0.5} \qquad (3)$$

where Z_e and Z_o are the characteristic impedances of the even and odd modes. Note that to minimize reflections at the near end of the turn in Fig. 2*b*, it was necessary to ensure the fulfillment of condition (3) just in segment 1. Also note that in this turn, since the conductors of segments have different parameters, part of the mode pulse energy is reflected from the junction between the segments and come to the turn output. The amplitudes of the reflected components are determined by the reflection coefficient for even and odd modes. They depend on the geometric mean of the characteristic impedance of the modes of the second segment. This happens because the first segment parameters are chosen to ensure condition (3). To clearly demonstrate reflections, the cross-section parameters of the second segment were chosen so that the amplitude of the reflected components is half of main mode component amplitudes.

To preliminarily simulate the turns in the time domain, we used a quasi-static approach in the TALGAT system [19]. This approach assumes that only transverse T-waves propagate in the structure and does not consider higher types of waves [20]. Thus, the Maxwell's equations are reduced to Poisson's equation. Consequently, the simulation task was reduced to finding the matrices of per-unit-length **RLCG**-parameters. Based on them, the response of a structure of finite length was calculated using telegraphic equations. In the case when losses in conductors and dielectric were not taken into account, only matrices **L** and **C** were calculated. This allows quasi-static analysis to be carried out much faster than a full-wave (or electrodynamic) approach.

As a substrate for the one- and two-segment turns, we chose the material with core thickness h=250 mm, foil thickness t=0.05 mm, and relative permittivity ε_r=11.2. To ensure condition (3), we chose the following width of the signal conductors and distance between them: w=0.17 mm and s=0.2 mm. The parameters of segment 1 of two-segment turn were chosen the same as for the turn in Fig. 2*a* to ensure condition (3). Parameters of segment 2 were the following: w_2=0.95 mm and s_2=1 mm. The calculated matrices **L** and **C** for such sets of turn parameters are summarized in Table I. The calculated per-unit-length delays of even and odd modes of the ML on Fig. 2*a* and segment 1 of a turn on Fig. 2*b* are τ_{o1}=7.63 ns/m and τ_{e1}=8.94 ns/m. And for the segment 2 they are τ_{o2}=9.96 ns/m and τ_{e2}=10.02 ns/m.

TABLE I
Calculated L and C Matrices

	L, nH/m	**C**, pF/m
Fig. 2*a*, Fig. 2*b* (first segment)	$\begin{bmatrix} 433.95 & 123.70 \\ 123.70 & 433.95 \end{bmatrix}$	$\begin{bmatrix} 165.53 & -22.20 \\ -22.20 & 165.53 \end{bmatrix}$
Fig. 2*b* (second segment)	$\begin{bmatrix} 113.15 & 2.83 \\ 2.83 & 113.15 \end{bmatrix}$	$\begin{bmatrix} 899.29 & -1.71 \\ -1.71 & 899.29 \end{bmatrix}$

First, consider the case when conditions (1) and (2) are not fulfilled. For this purpose, we took the total length of the ML from Fig. 2*a* of l=75 mm, and the length of segments 1 and 2 of 70 and 5 mm, respectively. As an excitation, we used a trapezoidal pulse with the electromotive force (e.m.f.) with an amplitude of 2 V and the front, fall, and flat top durations of 100 ps (Fig. 3). The main energy of excitation is concentrated in the frequency range up to 10 GHz. Fig. 4 shows the voltage waveforms at the input and output of the ML turns when conditions (1) and (2) are not met. The signal at the ML output in each case is distorted, and the excitation does not decompose into components. The signal amplitude at the output of the one-segment ML is 512 mV, and that of the two-segment ML is 563 mV.

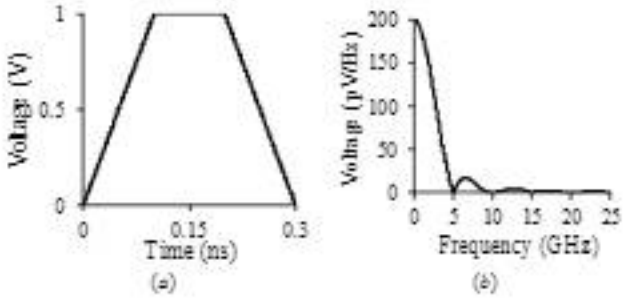

Fig. 3. UWB pulse: e.m.f. waveform (a) and voltage spectral density (b)

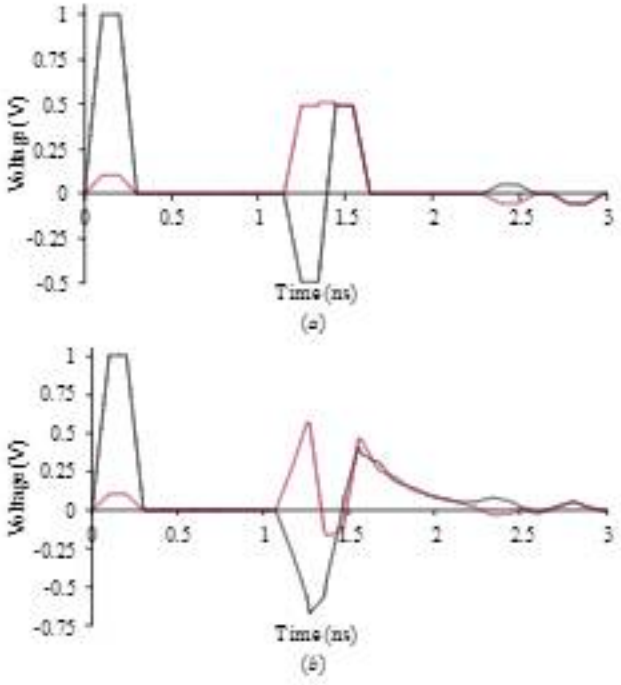

Fig. 4. Voltage waveforms at the input (–) and output (–) of the ML turns of one (a) and two (b) segments when conditions (1) and (2) are not met.

To ensure condition (1), the length of one-segment turn was chosen as l=118 mm. The lengths of segments of the two-segment turn were chosen l_1=l_2=100 mm to ensure condition (2). Fig. 5 shows the voltage waveforms at the input and output of the ML turns under study. Fig. 5*a* demonstrates that at the output of the one-segment turn, only two main decomposition pulses of smaller amplitudes are observed. They are pulses P_o and P_e of odd and even modes, respectively. In the two-segment turn, pulses P_o and P_e are decomposed into six main pulses due to the influence of reflections from the junction between the segments (Fig. 5*b*). The first two pulses (P_{or} and P_{er}) are the odd and even mode pulses reflected from the junction and arrived at the output. The second two pulses (P_o and P_e) are the main mode pulses that arrived at the output. The last two pulses (P_{o2r} and P_{e2r}) are the mode pulses reflected twice from the junction and arrived at the output. The signal amplitude at the output of the ML from Fig. 2*a* was 495 mV, and that of the ML from Fig. 2*b* was 433 mV.

We propose two cases of using the reflected components to reduce the amplitude of the output signal. Since the components reflected from the junction (P_{or} and P_{er}) and the main (P_o and P_e) have the largest amplitudes, the first case is their alignment by choosing the reflection coefficient between the segments. For this purpose, it is necessary to obtain the conditions of equality of component amplitudes and perform parametric optimization of the ML. In the second case, the reflected pulses of negative polarity (P_{er} and P_{o2r}) arrive simultaneously and are offset by basic mode pulses (P_o and P_e). For this case, it is also necessary to obtain the conditions for such arrival and perform parametric optimization of the cross-sections and lengths of the ML segments.

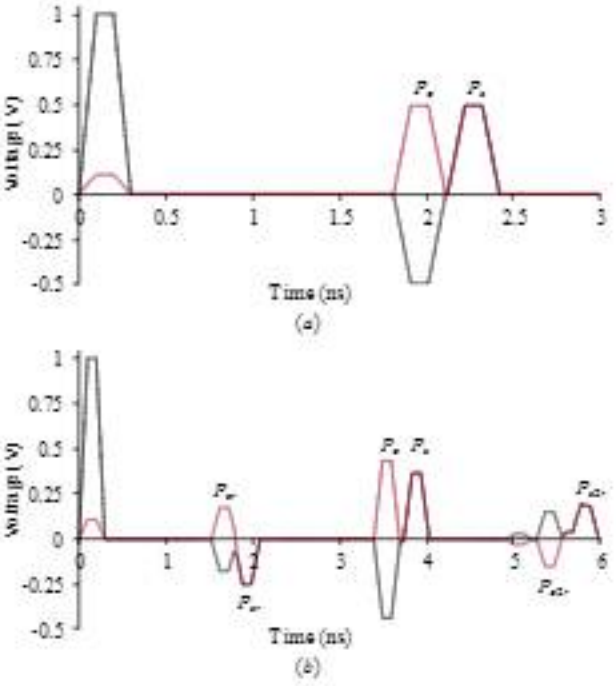

Fig. 5. Voltage waveforms at the input (–) and output (–) of the ML turns of one (a) and two (b) segments when conditions (1) and (2) are met.

III. Criteria for Optimizing Cross-Section Parameters

A. Signal Propagation Analysis Using Lattice Diagrams

First, let us consider the case of choosing the optimal matching between the segments to align the amplitudes of components P_{or}, P_{er} and P_o, P_e. For this purpose, we present lattice diagrams for each mode, which take into account only one reflection from the far end of the structure (Fig. 6). Based on these diagrams, we obtained the conditions that provide pulse attenuation for each of the proposed cases of using reflections in the two-segment ML.

B. The Condition of Equality of Amplitudes of the Main and Reflected Components

Based on the diagrams from Fig. 6, we obtained expressions defining each of the main components at the ML output

$$U_{or} = U_g \Gamma_{g12} T_{2o}, \qquad (4)$$

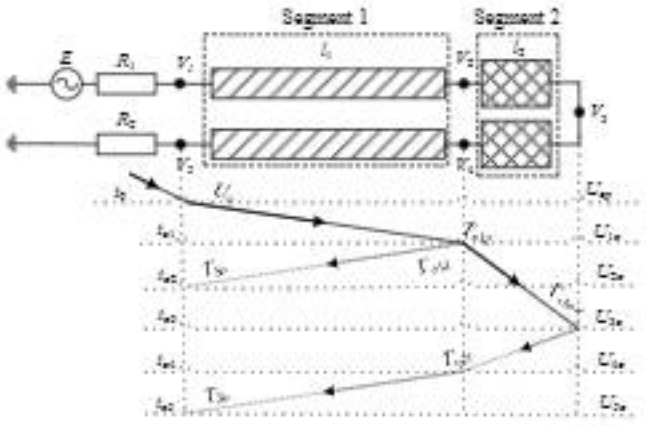

(a)

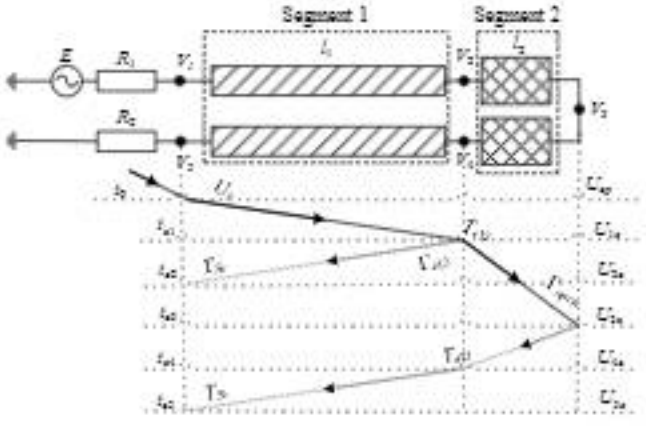

(b)

Fig. 6. Lattice diagrams of the odd (a) and even (b) modes in the ML turn of two segments

$$U_{o'} = U_o \Gamma_{o12} T_{2o1} \tag{5}$$

$$U_o = U_o T_{o12} T_{2o} \Gamma_{short} T_{o21} \tag{6}$$

$$U_e = U_e T_{e12} T_{2e} \Gamma_{open} T_{e21} \tag{7}$$

where Uo and Ue are the amplitudes of the incident wave of even and odd modes at the junction between the source and the first line segment, $T_{e,o}$ and $\Gamma_{e,o}$ are transmission and reflection coefficients for even and odd modes at the junction, and Γ_{open}=1, Γ_{short}=–1 for the far end of the ML turn.

We obtained $T_{e,o}$ and $\Gamma_{e,o}$ coefficients at the turn junctions using the mode decomposition technique in time domain from [22]. Now we need to equate expressions (4) and (6) first, and then expressions (5) and (7). Since the even mode pulse reflected from the junction between the segments has negative polarity, expression (5) should be multiplied by –1. After all substitutions and algebraic transformations, we obtain two identical quadratic equations

$$k^2 - 4k - 1 = 0 \tag{8}$$

where $k=Z_{o1}/Z_{o2}$ and $k=Z_{e1}/Z_{e2}$ for the first and second equations, respectively, characterizing the relationship between the impedances of odd and even modes of segments 1 and 2.

Equation (8) has one physical root k=2+√5. Then, the relationship between the geometric mean impedances of even and odd modes of segments 1 and 2 will be determined by the following relation

$$\frac{\sqrt{Z_{o1}Z_{e1}}}{\sqrt{Z_{o2}Z_{e2}}} = 2+\sqrt{5} \tag{9}$$

which ensures equality of modules of the amplitudes reflected from the junction of segments and the main pulses of odd and even modes at the output of the two-segment ML.

C. Conditions for Mutual Compensation of the Main and Reflected Components

In order for the reflected pulses of negative polarity to offset the pulses of modes, it is necessary to ensure their simultaneous arrival. Therefore, let us consider the conditions for selecting the lengths of segments 1 and 2. The optimization criteria was the simultaneous arrival of pulses P_{er} and $P_{o'}$ and P_o and P_{e2r}. We determined the arrival time of each main pulse in Fig. 5b by

$$t_{o'} = 2l_1\tau_{o1}, \tag{10}$$

$$t_o = 2l_1\tau_{o1} + 2l_2\tau_{o2}, \tag{11}$$

$$t_e = 2l_1\tau_{e1} + 2l_2\tau_{e2}, \tag{12}$$

$$t_{e2r} = 2l_1\tau_{o1} + 4l_2\tau_{o2}. \tag{13}$$

For pulses P_{er} and P_o to arrive simultaneously, we need to ensure the equality of (10) and (11), and for pulses P_e and P_{o2r} – the equality of (12) and (13). Moreover, their equality must be ensured simultaneously. After transforming the equality of equations (10) and (11), we obtained the condition

$$l_1(\tau_{e1} - \tau_{o1}) = l_2\tau_{o2} \tag{14}$$

and from the equality of equations (12) and (13), we obtained

$$l_1(\tau_{e1} - \tau_{o1}) = l_2(2\tau_{e2} - \tau_{o2}). \tag{15}$$

As we can see from conditions (14) and (15), their simultaneous fulfillment is possible only if τ_{o2} and τ_{e2} are equal. In inhomogeneous dielectric filling, the equality of (14) and (15) is possible, for example, by applying a varnish layer of high relative permittivity to the MSL surface. Then, for the MSL structure without varnish layer by choosing the segment lengths, we needed to ensure the approximate equality of the right sides of (14) and (15).

IV. Simulation Results

A. Equality of the Component Amplitudes

First, we consider the case when the amplitudes of reflected ($P_{o'}$, P_{er}) and main (P_o, P_e) components are equal. As a result of para-

metrical optimization according to criteria (2), (3), and (9), we obtained the following cross-sectional parameters for segments 1 and 2: w_1=0.18 mm, w_2=1.8 mm, s=0.05 mm, s_1=0.4 mm, s_2=0.15 mm, h=0.25 mm, and ε_r=11.2. The lengths of segments were l_1=125 and l_2=25 mm. The set of the cross-sectional parameters produces matrices **L**, **C**, and **Z**, which are summarized in Table II.

TABLE II
Calculated L, C, and Z Matrices for the First Case

	Segment 1	Segment 2
L, nH/m	$\begin{bmatrix} 429.78 & 67.10 \\ 67.10 & 429.78 \end{bmatrix}$	$\begin{bmatrix} 118.59 & 1.82 \\ 1.82 & 118.59 \end{bmatrix}$
C, pF/m	$\begin{bmatrix} 166.70 & -7.00 \\ -7.00 & 166.70 \end{bmatrix}$	$\begin{bmatrix} 827.35 & -36.19 \\ -67.49 & 813.35 \end{bmatrix}$
Z, Ω	$\begin{bmatrix} 50.73 & 5.04 \\ 5.04 & 50.73 \end{bmatrix}$	$\begin{bmatrix} 11.96 & 1.18 \\ 1.18 & 11.96 \end{bmatrix}$

To check the fulfillment of condition (2), we calculated per-unit-length delays of even and odd modes of segments 1 and 2: τ_{e1}=8.907 ns/m and τ_{o1}=7.937 ns/m; τ_{e2}=10.4 ns/m and τ_{o2}=9.3 ns/m. The left part of expression (2) is 0.297 ns; therefore, condition (2) is fulfilled with an error of 0.1%. In order to check the fulfillment of condition (3), we calculated the value of the geometric mean of the wave impedances of even and odd modes of segment 1, which was 50.48 Ω. Thus, condition (3) is satisfied with a deviation of less than 1%. In order to check condition (9), the left part of (3) was calculated, which was 11.9 Ω. Then the ratio of geometric mean products of even and odd modes of segments 1 and 2 is 4.24. This value is quite close to the value of the right part of (9), which is 4.23. The value is optimal, since it provides the alignment of the amplitude modules for the four main decomposition pulses at the line output.

Quasi-static and electrodynamic simulations were carried out in the time domain (Fig. 7). For full-wave analysis, we employed the finite difference method in the time domain (FDTD) [22] realized in the EMPro software. Losses in conductors and dielectrics were taken into account. Fig. 7 shows the voltage waveforms at the output of the two-segment ML when the parameters of segments 1 and 2 are optimal and ensure fulfillment of conditions (2), (3), and (9).

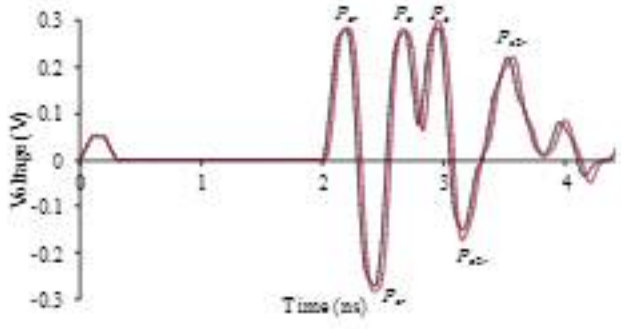

Fig. 7. Voltage waveforms at the ML output obtained by quasistatic (–) and electrodinamic (–) approaches when conditions (2), (3), and (9) are fulfilled.

The voltage waveforms obtained by different methods illustrate good agreement. The voltage waveform at the ML output is represented by a sequence of four basic pulses with close amplitudes. Slight differences in amplitudes and delays can be explained by differences in the numerical methods underlying the simulation approaches. Another reason for the differences can be radiation losses, which are not taken into account in the quasi-static simulation. The total losses lead to a delay in the rise and fall times of the response components, which leads to a decrease in the duration of the flat top. For a more detailed quantitative evaluation, Table III summarizes the amplitudes and delays (at half the amplitude level) of the decomposition pulses at the ML output.

TABLE III
Pulse Amplitudes (mV) and Delays (ns) for Fig. 7

U_1	U_2	U_3	U_4	t_1	t_2	t_3	t_4
Quasi-static approach							
280.6	272.2	274.3	282.7	2.023	2.293	2.533	2.773
Electrodynamic approach							
286.3	286.0	283.8	300.3	2.013	2.323	2.563	2.823

Table III shows that the maximum difference between the amplitudes and delays of the components does not exceed 17.6 mV and 0.05 ns, respectively, which can be considered acceptable. The attenuation of the output signal amplitude according to the results of the quasi-static simulation was 3.53 times (relative to half of the source e.m.f. amplitude), and the electrodynamic – 3.33 times.

To assess the danger of input and decomposed voltage waveforms, we used *N*-norms [23]. Table IV shows the names, formulas, and descriptions of each norm reproduced from [24].

TABLE IV
N-norms of a Waveform

Norm	Name	Equation	Application
N_1	Peak value (absolute)	$\lvert U(t)\rvert_{max}$	Circuit upset / electric breakdown / arcover effects
N_2	Peak derivative (absolute)	$\left\lvert \frac{dU(t)}{dt} \right\rvert_{max}$	Component arcing / circuit upset
N_3	Peak pulse (absolute)	$\left\lvert \int_0^t U(t)dt \right\rvert_{max}$	Dielectric puncture (if U denotes E field)
N_4	Rectified general pulse	$\int_0^T \lvert U(t)\rvert dt$	Equipment damage
N_5	Square root of the action integral	$\left\{ \int_0^T \lvert U(t)\rvert^2 dt \right\}^{\frac{1}{2}}$	Component burnout

*$U(t)$ is the voltage waveform

In Table V, we summarize the *N*-norm values for the input and output of the turn of two segments calculated from the results of different approaches. Additionally, we include the results of *N*-norm calculations based on the quasi-static simulation results of the turn of one segment with initial parameters (like those of segment 1).

From Table V, we can see that the values of all norms obtained at the output of the devices are significantly lower than for the initial

excitation at the input. The decrease in N_1 for one turn (without reflections) was 2.1 times, and N_2 – 2.24. There is no reduction of in N_3, while N_4 and N_5 decrease by 1.8 times. By comparing N-norms obtained for the ML of one and two segments by quasi-static approach, we can see that reflections allow a decrease in the value of N_1 by 1.66 times, but at the same time lead to an insignificant growth of N_2 and more significant growth of N_4. Note that in the case of N_3 and N_5, no attenuation was observed, since the energy of 2 pulses (in the turn of one segment) is distributed over 4 pulses (in the turn of two segments). The total reduction in N_1 as a result of decomposition and the use of reflections was 3.5 times. Also note that the decrease in N_2 is not so significant and is only 1.9 times. Similar values were obtained for the responses calculated as a result of electrodynamic simulation. This indicates the consistency and correctness of the results obtained by the two approaches. However, the values of the norms obtained based on the results of electrodynamic simulation turned out to be higher.

TABLE V

Calculated N-norms for Fig. 7

Source data	N_1	$N_2 \cdot 10^{-9}$	$N_3 \cdot 10^{10}$	$N_4 \cdot 10^{10}$	$N_5 \cdot 10^3$
Quasi-static approach (one segment)					
Input	0.997	9.966	2.015	3.817	1.509
Output	0.471	4.442	1.984	2.150	0.859
Quasi-static approach (two segments)					
Input	0.997	9.966	2.027	5.722	1.535
Output	0.284	5.284	1.997	3.527	0.778
Electrodynamic approach (two segments)					
Input	0.983	9.978	2.026	5.862	1.532
Output	0.303	5.636	1.939	3.756	0.815

B. Mutual Compensation of Response Components

Now, we consider the case of mutual compensation of the main and reflected components. We use the per-unit-length delays of even and odd modes of the segments from Section II. Thus, we optimize only segment lengths. They are l_1=100 mm and l_2 = 14.89 mm. They ensure approximate equality of the right sides of conditions (14) and (15). Quasi-static and electrodynamics simulations were carried out in the time domain (Fig. 8).

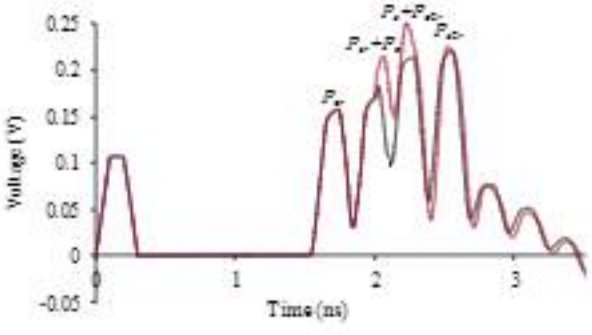

Fig. 8. Output voltage waveforms obtained by quasistatic (–) and electrodinamic (–) approaches when approximating equality of rigth sides of conditions (14) and (15).

It can be seen from Fig. 8 that the waveforms obtained by different approaches are in good qualitative agreement; they both consist of four main pulses. However, the waveforms differ quantitatively because of differences in the approaches. Deviations in the results can be explained by the effect of radiation losses. The expansion of decomposition pulses, as well as the increase in the amplitude of the output voltage in the electrodynamic approach can be caused by the superposition of pulses.

For a detailed quantitative evaluation, Table VI summarizes the calculated amplitudes and delays of the decomposition pulses. The amplitude of the output voltage in the quasi-static approach corresponds to the fourth pulse and equals 220.5 mV, while in the electrodynamic approach it corresponds to the third pulse and equals 250.5 mV. Deviations in the amplitudes and delays do not exceed 30 mV and 0.04 ns, respectively. Thus, the proposed approach makes it possible to additionally suppress the UWB pulse amplitude. This suppression is twice as big as in the turn of one segment.

TABLE VI

Pulse Amplitudes (mV) and Delays (ns) for Fig. 8

U_1	U_2	U_3	U_4	t_1	t_2	t_3	t_4
Quasi-static approach							
157.7	182.7	213.5	220.5	1.533	1.833	2.113	2.373
Electrodynamic approach							
146.8	215.2	250.5	225.6	1.563	1.873	2.153	2.393

In Table VII, we summarize the N-norm values for the input and output of the two-segment turn calculated from the results of different approaches, as well as quasi-static simulation results of the one-segment turn.

TABLE VII

Calculated N-Norms for Fig. 8

Source data	N_1	$N_2 \cdot 10^{-9}$	$N_3 \cdot 10^{10}$	$N_4 \cdot 10^{10}$	$N_5 \cdot 10^3$
Quasi-static approach (one segment)					
Input	0.995	9.948	2.013	4.008	1.520
Output	0.472	4.479	1.987	2.362	0.862
Quasi-static approach (two segments)					
Input	0.995	9.948	2.010	5.419	1.653
Output	0.221	2.175	1.983	2.381	0.534

It can be seen from Table VII that the calculated N-norm values for the turn of two segments are in good agreement and confirm the conclusions made earlier. Deviations in the results of N-norm calculations might have been caused by incomplete decomposition of the excitation. By comparing the results obtained for the turns of one and two segments, we can see that the values of N_1 and N_2 decreased by about 2 times. The cumulative results suggest the possibility of additional suppression of UWB pulse amplitudes by using reflections. Note that information signals, because of their relatively long duration, do not undergo distortions.

V. Signal Integrity Analysis

The signal integrity analysis is performed for the cases that use reflections. For each of the cases, as a result of electrodynamic

simulation, we obtained frequency dependences of the transmission and reflection coefficients magnitudes (|S21| and |S11|), as well as eye diagrams.

A. The Case of Equality of the Component Amplitudes

Fig. 9 shows frequency dependences of $|S_{21}|$ and $|S_{11}|$ obtained by the electrodynamic approach. They show that the cutoff frequency is 111 MHz. This suggests that useful signals with frequency up to 111 MHz will be subject to minimal distortions. The dependencies also show a degradation of the turn matching at higher frequencies.

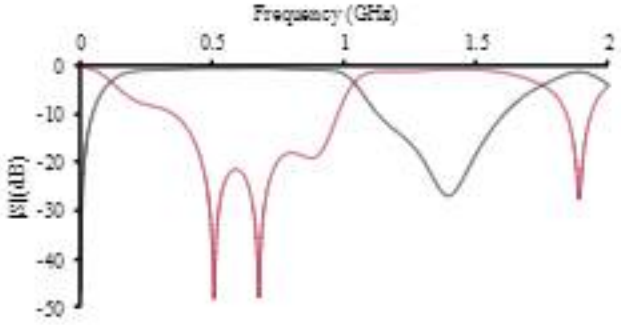

Fig. 9. Frequency dependences of $|S_{21}|$ (–) and $|S_{11}|$ (–) up to 2 GHz obtained for the case of equalization of the response components amplitudes.

Eye diagrams were calculated when a pseudo-random binary sequence (PRBS) was propagating with transmission rates of 75, 100, 125, and 150 Mbps (Fig. 10). These rates were chosen so that the height of the eye was at least 0.707 of the level of the useful signal at the ML output. The figures show a temperature view of the three-dimensional eye diagrams. The eyes are automatically centered and displayed at 2*T* on the horizontal axis. The colors of the eye diagram indicate the frequency of point crossings in the time-voltage plane. Frequent point crossings are characterized by lighter shades, and rarer ones by darker shades. In addition, constant error probability contours were estimated and superimposed on the diagrams in the form of BERContour. In addition to the graphical representation of the eye diagrams, their main parameters were estimated (Table VIII). The obtained results allow us to evaluate the fields of application of the proposed approach.

TABLE VIII
Useful Signal Parameters for the Case of Equalizing the Amplitudes of the Main and Reflected Components

Speed (Mbps)	Eye height (mV)	Eye width (ns)	JitterPP (ps)	SNR
75	932	13.13	0.	6.552
100	954	9	50	9.6
125	849	7.480	400	3.497
150	766	6.267	333.3	2.539

From the diagrams in Fig. 10, we can see that the ML under study provides the best transmission quality at the rates of up to 100 Mbps. A further increase in the rates of up to 125 and 150 Mbps leads to a deterioration of the eye characteristics. So, for example, at 100 Mbps, the jitter is 50 ps, and when the rate increases to 125 Mbps, the jitter is as high as 400 ps. Similar results were found when analyzing the SNR. By increasing the bit rate from 100 to 125 Mbps, the SNR decreases from 9.6 to 3.5. A further increase in the bit rate leads to an even greater decrease in SNR. Meanwhile, even at 150 Mbps the eye remains open, indicating a low probability of bit errors in signal transmission. However, due to a significant distortion of the signal waveform, the ML use at this speed is limited.

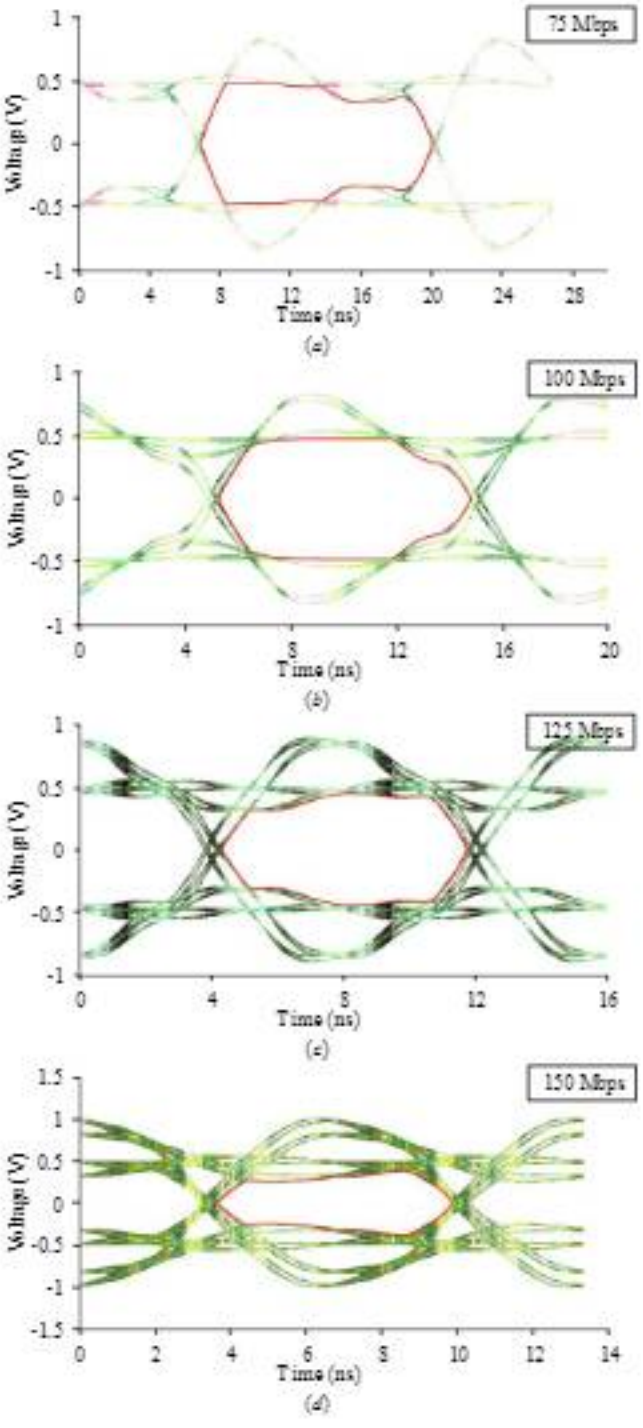

Fig. 10. Eye diagrams for the case of equalizing the amplitudes of the main and reflected components for 75, 100, 125, and 150 Mbps bitrates (a–d).

B. The Case of Mutual Compensation of Response Components

Fig. 11 shows frequency dependences of $|S_{21}|$ and $|S_{11}|$. It can be seen that the useful signals with boundary frequency less than 233.5 MHz will be subjected to minimal distortions.

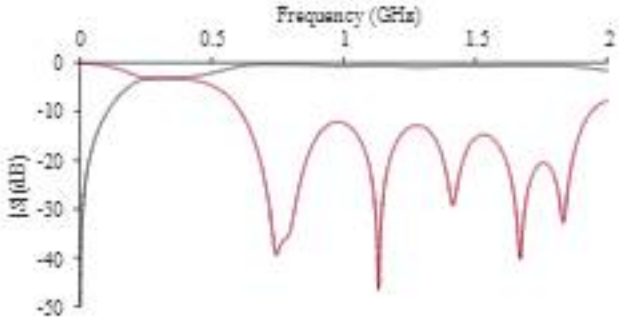

Fig. 11. Frequency dependences of $|S_{21}|$ (–) and $|S_{11}|$ (–) up to 2 GHz obtained for the case of mutual compensation of the main and reflected components.

Fig. 12 shows the eye diagrams at PRBS for transmission rates of 150, 175, 200, and 225 Mbps. As before, these rates were chosen with the consideration that the height of the eye is at least 0.707 of the level of the useful signal. The results of processing and interpretation of the diagrams are summarized in Table IX.

TABLE IX
Useful Signal Parameters for the Case of Mutual Compensation of the Main and Reflected Components

Speed (Mbps)	Eye height (mV)	Eye width (ns)	JitterPP (ps)	SNR
150	972	6.533	10	6.879
175	972	5.571	11.43	5.036
200	958	4.8	17.5	4.195
225	869	4.2	22.22	3.249

A comparison of the results presented in Tables VIII and IX for 150 Mbps shows that all parameters of the eye diagram (except for the width) obtained for case 2 are significantly better. The jitter is only 10 ps, and the SNR value is 6.88. A further increase in the bit rate leads to a deterioration of the eye parameters, but even at 225 Mbps they are quite high. Note that when the bit rate is increased from 150 to 225 Mbps, the jitter does not increase significantly (from 10 to 22 ps), but the SNR value decreases by more than 2 times. Meanwhile, such results at fairly high speeds can be considered acceptable. Even at 225 Mbps, the eye is open, which indicates a low probability of bit errors. The aggregate of the results suggests that the second case is preferable, both in terms of attenuation and operating bandwidth, and in terms of signal integrity.

VI. Example of Practical Application of the Approach

As an example, we chose a PCB based on the Raspberry Pi 2040 (RP2040) microcontroller (Fig. 13). Since we only aimed to demonstrate an example of how to place an ML-turn-based protection device on a PCB, we do not provide a detailed description of the device and the PCB. The device is shown in red color in the right upper part of the PCB, and the case involves mutual compensation of response components. To protect against UWB interference, the ML turn occupying a free space of a PCB is connected in the power supply circuit, between the USB-C connector and the microcontroller power subsystem. The cross-section parameters of the turn correspond to those used above (Fig. 8), and the total length of the turn is assumed to be half as long (55.44 mm).

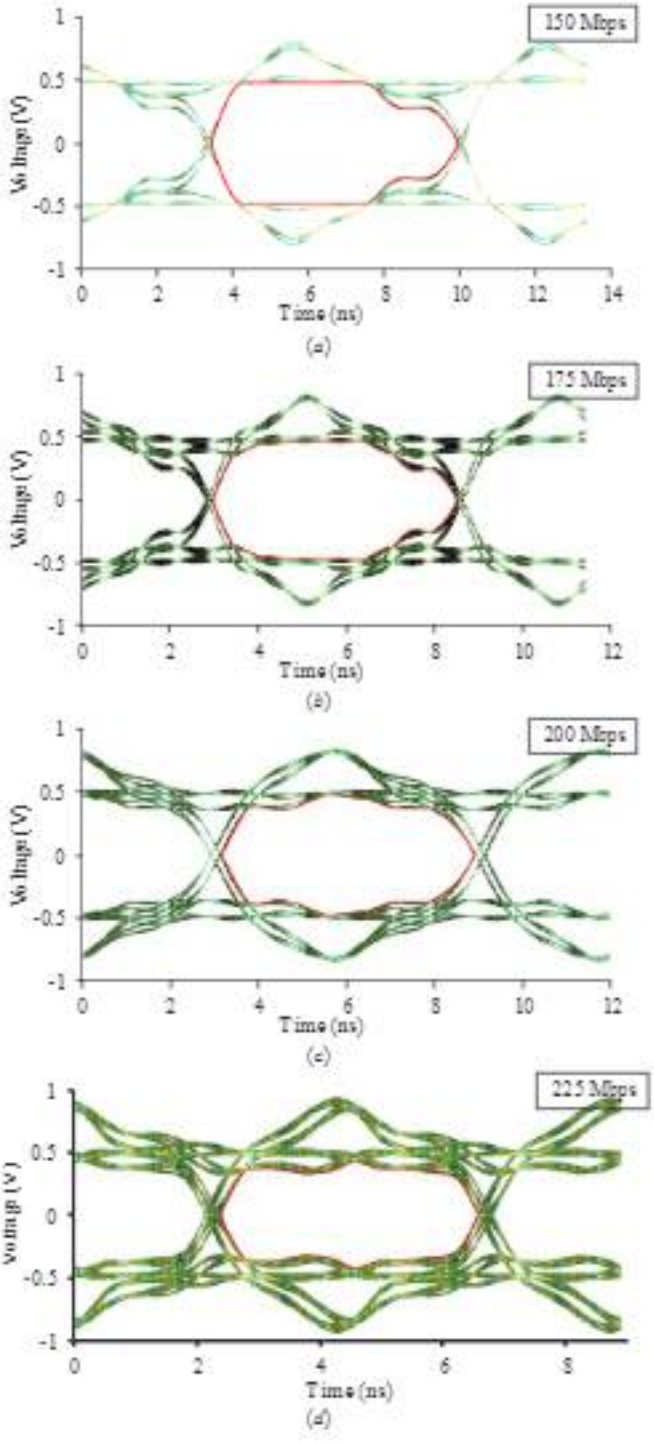

Fig. 12. Eye diagrams for the case of mutual compensation of the main and reflected components at 150, 175, 200, and 225 Mbps bitrates (a–d).

Electrodynamic simulation was performed to obtain the time response at the output of a turn. Fig. 14 shows the voltage spectral density and voltage waveform of a Gaussian UWB pulse with e.m.f. amplitude of 2 V and duration of 67 ps by 0.5 level [25], and voltage waveform at the output of the ML turn based protection device.

Fig. 14*a* shows that the spectral density of the interference has significantly decreased, especially in the frequency range of 2–7 GHz. Fig. 14*b* shows that the interfering excitation is decomposed into a sequence of components with the amplitudes of less than 220 mV. Since the turn is twice as short, the full effect of superposition of the main and reflected components is not observed.

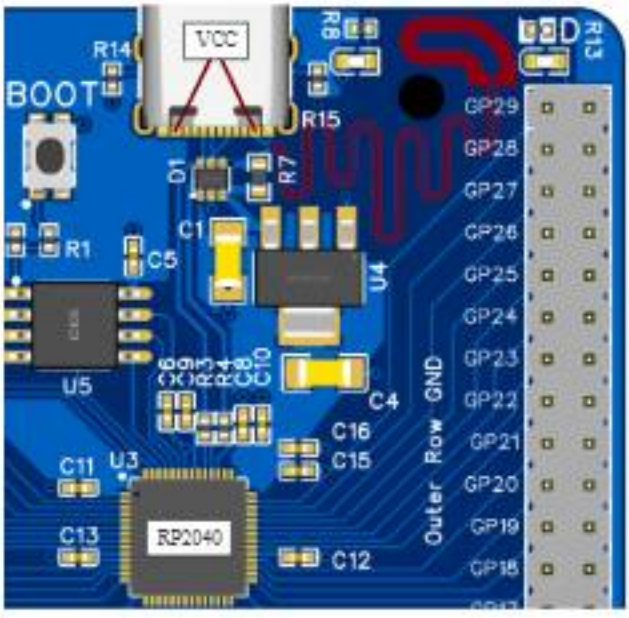

Fig. 13. Example of practical application of the reflections

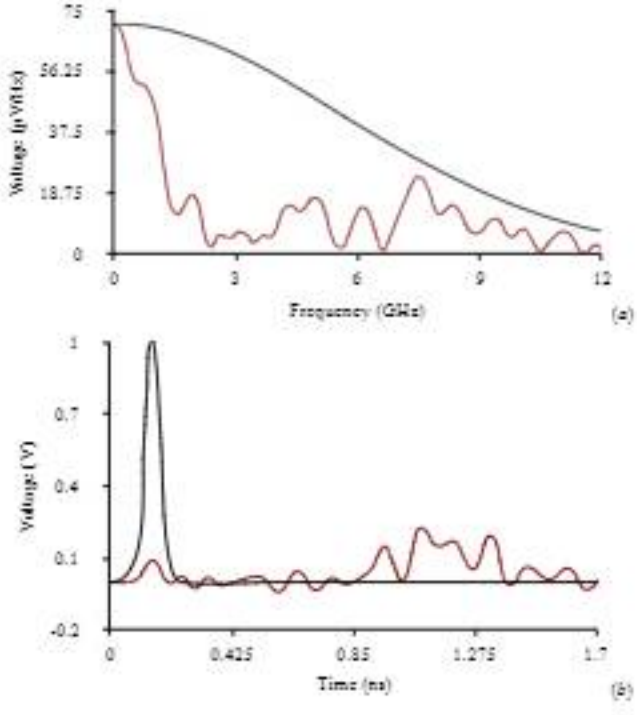

Fig. 14. Gaussian pulse voltage waveforms and voltage spectral density at the input (–) and output (–) of ML turn

When designing such devices, it is necessary to have enough free space on the PCB. In addition, in their design it is necessary to take into account additional signal delay. These two factors can limit the use of devices in high-speed circuits, but allows their use in power supply circuits for pre-filtering and minimizing the influence of UWB interference.

VII. Conclusion

In this paper, the possibility of suppressing the amplitude of pulsed UWB interference have been considered in strip devices in the form of MLs of two segments. These devices are based on the phenomenon of decomposition of the interfering signal into components due to the difference in propagation velocities of these components. The use of reflections between segments caused by their mismatch has been proposed. For this purpose, two possible cases of reducing the interfering signal amplitude were considered. The first one is based on the alignment of amplitudes of the main and reflected components at the ML output. For this, we obtained the condition determining the relationship between values of geometric mean of wave impedances of even and odd modes for segments 1 and 2. The second case is based on simultaneous arrival and mutual compensation of the main and reflected components. For this case, we obtained the conditions in the time domain, which provide the simultaneous arrival and superposition of the components.

The voltage waveforms at the output of the studied ML have been simulated for each case. As a result, it was found that case 1 provides attenuation up to 3.5 times, and case 2 – up to 3.9 times. This confirms the possibility of an additional decrease in the amplitude of the UWB excitation by means of reflections from the junction between the segments.

N-norms, characterizing the susceptibility of REE to UWB excitation, were evaluated. The evaluation results also confirm the possibility of using reflections.

Finally, eye diagrams were calculated for the PRBS propagating in the turn to assess the integrity of the useful signal. As a result, it was found that case 1 can be used for signal transmission at the rates up to 150 Mbps. However, due to significant distortions of the signal waveform, the use of the ML at this speed is limited (SNR was 2.5). For case 2, the best parameters of the eye diagram were obtained at 150 Mbps (SNR was 6.8). It is shown that case 2 is applicable at bit rate up to 225 with rather low jitter and acceptable SNR reduction. The comparative analysis of eye diagrams for the two cases indicates the preference of the case of mutual compensation of the response components. It provides more significant suppression of UWB excitations and ensures signal integrity at higher data rates at a fairly small degradation of the characteristics of the eye diagram.

To visually demonstrate how the device can be implemented on a real PCB, we provided an example of the proposed approach.

References

1. IEC 61000-4-3:1995. "Electromagnetic compatibility," – Testing and measurement techniques – Radiated, radio-frequency, electromagnetic field immunity test. June 1998.
2. F. Sabath, "A systematic approach for electromagnetic interference risk management," IEEE Electromagnetic Compatibility Magazine, vol. 6, no. 4, pp. 99–106, 2017.
3. D.V. Giri, R. Hoad, and F. Sabath, "Implications of high-power electromagnetic (HPEM) environments on electronics," IEEE Electromagnetic Compatibility Magazine, vol. 9, no. 2, pp. 37–44, 2020.
4. L.C. Lavau, M. Suhrke and P. Knott, "Susceptibility of sensors to IEMI," IEEE Int. joint EMC/SI/PI and EMC Europe symposium, pp. 533–537, Oct. 2021.
5. W. A. Radasky, "Fear of frying electromagnetic weapons threaten our data networks. Here's how to stop them," in IEEE Spectrum, vol. 51, no. 9, pp. 46-51, Sept. 2014.
6. J. Lehr and P. Ron, "Foundations of Pulsed Power Technology," Hoboken, NJ, USA: Wiley, 2017.
7. L. Devaraj, A. R. Ruddle, and A. P. Duffy, "Electromagnetic risk analysis for EMI impact on functional safety with probabilistic graphical models and fuzzy logic," IEEE Letters on Electromagnetic Compatibility Practice and Applications, vol. 2, no. 4, pp. 96–100, Dec. 2020.
8. J. Galvis, D. Martinez, G. N. Appiah, F. Albarracin, C. Kasmi, and N. Mora, "Efficient estimation of the band ratio of HPEM sources for IEME classification," IEEE Lett. Electromagnet. Compat. Pract. Appl.,vol. 4, no. 1, pp. 7–10, Mar. 2022.
9. X.C. Wang, Y.Y. Sun, J.H. Zhu, Y.H. Lou, and W.-Z. Lu, "Folded feedthrough multilayer ceramic capacitor EMI filter," IEEE Transactions on Electromagnetic Compatibility, vol. 59, no. 3, pp. 996–999, June 2017.
10. J. Baek, Y. Cho, and K. Ko, "Analysis of design parameters reducing the damage rate of low-noise amplifiers affected by high-power electromagnetic pulses," IEEE Trans. Plasma Sci., vol. 46, no. 3, pp. 524–529, Mar. 2018.
11. X. Dai, W. Feng, and W. Che, "Investigation and improvements of UWB microstrip delay lines," IEEE Trans. Compon., Packag., Manuf. Technol., vol. 11, no. 8, pp. 1292–1300, Aug. 2021.
12. L. Huang and S. Zhang, "Ultra-wideband ridged half-mode folded substrate integrated waveguide filters," IEEE Microw. Wireless Compon. Lett., vol. 28, no. 7, pp. 579–581, Jul. 2018.
13. C.-J. Chen, "Design of artificial transmission line and low-pass filter based on aperiodic stubs on a microstrip line," IEEE Trans. Compon., Packag. Manuf. Technol., vol. 4, no. 5, pp. 922–928, May 2014.
14. V. Radonic and V. Crnojevic-Bengin, "Super-compact stopband filter based on grounded patch resonator," Electronics Letters, vol. 46, no. 2, pp. 146–147, 2010.
15. D. Packiaraj, K. J. Vinoy, M. Ramesh, and A. T. Kalghatgi, "Analysis of multiconductor coupled microstrip lines with an aperture in the ground plane for the design of a broadband filter," Journal of Electromagnetic Waves and Applications, vol. 27, no. 7, pp. 856–867, Apr. 2013.
16. X. Wu, Y. Li, and X. Liu, "Quasi reflectionless microstrip bandpass filters with improved passband flatness and out-of-band rejection," IEEE Access, vol. 8, pp. 160500–160514, 2020.
17. A.T. Gazizov, A.M. Zabolotsky, and T.R. Gazizov, "UWB pulse decomposition in simple printed structures," IEEE Trans. Electromagnet. Compat., vol. 58, no. 4, pp. 1136–1142, Aug. 2016.
18. R.S. Surovtsev, A.V. Nosov, A.M. Zabolotsky and T.R. Gazizov, "Possibility of protection against UWB pulses based on a turn of a meander microstrip line," IEEE Transactions on Electromagnetic Compatibility, vol. 59, no 6, pp.1864–1871, 2017.
19. S.P. Kuksenko, T.R. Gazizov, A.A. Kvasnikov, A.V. Demakov, A.A. Ivanov, D.V. Klukin, A. Alhaj Hasan, A.E. Maksimov, and A.V. Osintcev, "Developing software for modelling radioelectronic equipment with respect to electromagnetic compatibility in TUSUR," Nanoindustry, vol. 16, no S9-1(119), pp.170–178, 2023.
20. J.D. Jackson. "Classical electrodynamics", New York, John Wiley & Sons, pp. 641, 1962.
21. Park S.W. Analytical approach for crosstalk characterization of multiconductor transmission lines using mode decomposition technique in the time domain / S.W. Park, F. Xiao, Y. Kami // IEEE Transactions On Electromagnetic Compatibility. – 2010. – Vol. 52. – pp. 436–446.
22. K.S. Yee, "Numerical solution of initial boundary value problems involving Maxwell's equations in isotropic media," IEEE Transactions on antennas and propagation, vol. 14, no. 3, pp. 302–307, 1966.
23. IEC 61000-1-5: "Electromagnetic compatibility (EMC) – Part 1-5: High power electromagnetic (HPEM) effects on civil systems," Ed. IEC, 2004. C.E. Baum, "Norms and eigenvector norms," Mathematics Notes, vol.63, pp. 1–42, 1979.
24. D. Giri, "High-power electromagnetic radiators: nonlethal weapons and other applications," Cambridge MA: Harvard University Press, pp. 212, 2004.

Biographies

Roman S. Surovtsev *was born in 1991. He received the engineering degree in 2013, and the Ph.D. degree in 2016. Currently he works as a senior researcher at the "Safety and Electromagnetic Compatibility of Electronic Equipment" laboratory and as an assistant professor at Tomsk State University of Control Systems and Radioelectronics (TUSUR). He has authored more than 150 scientific papers, including three books.*

Pavel V. Mikola *was born in 1998. He received the B.Sc. and M.Sc. degree in Infocommunication Technologies and Communication Systems from TUSUR in 2020 and 2022, respectively. Currently he is a Ph.D. student and a junior research fellow at TUSUR. He has authored/coauthored six scientific papers. His research interests include electromagnetic compatibility and protection against UWB excitations.*

Salim Karri *was born in 1996. He received the B.Sc. and M.Sc. degree in Infocommunication Technologies and Communication Systems from TUSUR in 2018 and 2020, respectively. Currently he is a Ph.D. student and a junior research fellow at TUSUR. He has authored/coauthored 15 scientific papers. His research interests include electromagnetic compatibility, design of protecting devices, and signal integrity.*

Ilya A. Ivantsov *was born in 1998. He received the B.Sc. and M.Sc. degree in Infocommunication Technologies and Communication Systems from TUSUR in 2020 and 2022, respectively. Currently he is a Ph.D. student and a junior research fellow at TUSUR. He has authored/coauthored 10 scientific papers. His research interests include electromagnetic compatibility.* **EMC**